

# Probability Map Guided Bi-directional Recurrent UNet for Pancreas Segmentation

Jun Li<sup>†</sup>, Xiaozhu Lin<sup>†</sup>, Hui Che, Hao Li, and Xiaohua Qian<sup>\*</sup>

**Abstract**—Pancreatic cancer is one of the most lethal cancers as incidence approximates mortality. A method for accurately segmenting the pancreas can assist doctors in the diagnosis and treatment of pancreatic cancer. In the current widely used approaches, the 2D method ignores the spatial information of the pancreas, and the 3D model is limited by high resource consumption and GPU memory occupancy. To address these issues, we propose a bi-directional recurrent UNet (PBR-UNet) based on probability graph guidance, which consists of a feature extraction network for efficiently extracting pixel-level probability map as guidance and a bi-directional recurrent network for precise segmentation. The context information of adjacent slices is interconnected to form a chain structure. We integrate contextual information into the entire segmentation network through bi-directional loops to avoid the loss of spatial information in propagation. Additionally, an iterator is applied in the process of propagation, which is used to update the guided probability map after each propagation. We solve the problem that the 2D network loses three-dimensional information and combines the probability map of the adjacent slices into the segmentation as spatial information, avoiding large computational resource consumption caused by direct use of the 3D network. We used Dice similarity coefficients (DSC) to evaluate our approach on NIH pancreatic datasets and eventually achieved a competitive result of 83.02%.

**Index Terms**—CT, pancreas segmentation, deep learning

## I. INTRODUCTION

In traditional pancreatic cancer surgery, surgeons usually judge the anatomical structure of the human body by experience. However, due to the huge difference in the shape of the pancreas and the vulnerability to the elastic deformation such as breathing and heartbeat, it is hard to locate the pancreas. Therefore, exploring the automatic segmentation of the pancreas is of great significance for improving the accuracy and risk reduction of computer-assisted diagnosis techniques. DSC accuracy can reach more than 90% when segmenting the kidney, heart or liver [1], [2]. Compared with the segmentation of these organs, [3] and Figure 1 (a) show the smaller volume fraction and high anatomical variability of the pancreas, which

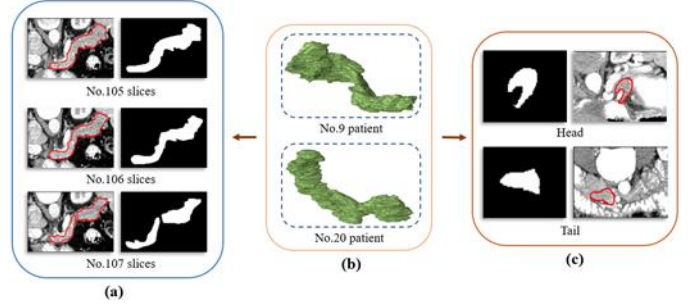


Fig. 1. Examples of CT scans showing pancreas. (a) indicates that the adjacent three-slice pancreas has a great correlation; (b) indicates that the pancreas of different individuals has different spatial shapes; (c) indicates the significant difference in shape between the head and tail of the patient's pancreas.

prevents many segmentation methods from achieving high precision [4] and making the model easily disturbed by background tissue or dramatic volume changes. Thus, the pancreas has always been considered one of the most difficult types of organ segmentation [5], [6].

In recent years, with the development of deep learning, more and more researchers began to use natural image semantic segmentation model to solve medical image segmentation tasks. Many excellent semantic segmentation models have been proposed in the past two years, such as FCN [7], UNet [8], DeepLab [9]. The structure of Encoder-Decoder is widely used in the field of medical image segmentation, because skipping connection has been proved to be helpful to restore the full spatial resolution of network output, making the full convolution method suitable for semantic segmentation [10], [11]. It turns out that a network with this structure not only increases the final output resolution but also enables accurate positioning. Because it can not only detect the semantic information of the target organization in the whole slice which means the difference between the target organization and other organizational features; it can also get more precise details features than FCN through Encoder. In the existing deep learning methods, most of them are still based on two-dimensional image segmentation, each slice of an organ is divided into segmentation objects. After the segmentation is completed, recombination is performed to generate the segmented three-dimensional organ [5], [12], [13]. This approach ignores the contextual information of the organ in the segmentation. In clinical diagnostics, experienced radiologists usually observe and segment the target tissue according to many adjacent slices along the Z axis [14]. However, 2D FCNs-based methods ignore the context on the Z axis. As can be seen from Figure 1(a), the difference in the target tissue in adjacent slices of medical images is relatively

J. Li, H. Li, and X. Qian, are with the School of Biomedical Engineering, Shanghai Jiaotong University, Shanghai 200240, China (e-mail: dirk.li@outlook.com; haoli@sjtu.edu.cn; xiaohua.qian@sjtu.edu.cn )

X. Lin is the Ruijin Hospital, Shanghai Jiaotong University School of Medicine, Shanghai 200240, China.

H. Che is the School of Biomedical Engineering, Rutgers University, New Brunswick 08901-1281, USA.

<sup>†</sup> J. Li and X. Lin contributed equally.

<sup>\*</sup> Xiaohua Qian is the corresponding author.

small, so we can try to use a range of adjacent slices to guide the segmentation of each slice.

There are also some researchers who use 3D models to directly treat all slices of a patient as a segmentation object [15]–[21], which does take advantage of the three-dimensional information of the organ, but this approach relies excessively on computing resources and high requirements for hardware devices [14], [22], resulting in high computational cost and GPU memory consumption. High memory consumption limits the depth of the network and the field of view of the filter, which is precisely the two key factors for performance improvement [23]. In [24], the researchers evaluated a complete 3D convolutional architecture and found that it provided a slightly higher result than the previous method, at the cost of a significant increase in computational capacity requirements. In this paper, it is possible to make the result lower by directly using all slices of a patient as a segmented object. It can be seen from Figure 1(c), the head and tail of the pancreas are not directly related, and there is no correlation in shape so that the segmentation results may be misled by the dramatic shape changes in the pancreas. Moreover, we notice that the similarity of adjacent slices is very high, so we use the adjacent slices as the segmentation guidance in this paper, we will discuss the details in the Discussion section.

The volume of the pancreas is small, the majority of the image is the background, and a single segmentation may cause the results to be biased towards the background, so some researchers have begun to try two-step segmentation [18], [25]–[28]. The pancreatic region is positioned by rough approximate segmentation, and then fine segmentation is carried out in the positioned area. With the first segmentation, most of the background interference can be removed, allowing the model to focus on segmentation within a specific range. However, this approach lacks an effective corrective measure. In the first step, the model will not only remove background interference but also possibly remove the correct pancreatic target tissue, which is irreversible. [29] shows us two failed examples of the proposed method by [5], in which even the output of DSC is 0. In this complicated situation, the positioning result is usually unreliable and unstable due to the lack of an effective error correction mechanism. Besides, in fine segmentation, it is generally difficult to utilize the third dimension of information, resulting in inaccurate segmentation performance [3].

After BiLSTM (Bi-directional Long Short-Term Memory) achieved great success in text analysis, researchers tried to introduce it into medical image segmentation [30], [31]. This approach treats the context information of the pancreas as a sequence, and the context information is given to different nodes in the BiLSTM, which can use spatial information to optimize the segmentation results. However, the drawback of this approach is still that the tortuosity of the shape of the pancreas may lead to wrong guidance. For example, if the pancreatic head is used to guide the tail of the pancreas, the result will greatly deviate. Moreover, for BiLSTM or LSTM, it is only a refine module connected to the main network [30], which has little contribution to the result, but makes the entire

network larger and the duration of the training longer. Compared to the computational resources it consumes, this kind of network with bi-directional long short-term memory has a limited contribution to the result.

Inspired by the above ideas, in this paper, we propose a more efficient model of bidirectional cyclic segmentation based on probability map guidance. First, we use the 2D Unet model to extract the pixel-level probability map in each slice. As described above, the probability generated here represents the probability of each pixel belonging to the pancreatic tissue. Although this probability map can identify the approximate location of pancreatic tissue in each slice, the accuracy is not guaranteed. However, we innovatively use it for the guidance of fine segmentation. As shown in Figure 1(a), the adjacent slices have a strong correlation, so we constrain the middle slice with the information of the adjacent slice positions of the current slice, patching and optimizing some of the pixels that were segmented incorrectly in the first step. Thus, making up for the shortcomings of using a binary map to describe only the outlines that cannot describe the details. Then, we used another multi-channel network to integrate the intra-slice and adjacent slice contexts, which proved to be better than a single-channel network without increasing the computational burden [24]. In the integration process, because the segmentation results will be affected by adjacent slices, and adjacent slices will be affected by other slices, the effect will be transmitted in all slices of the patient. To enable this interaction to propagate through the network and get the best results, we add an iterative process of two-way loops to optimize and update the probability maps in each propagation process. Under the guidance of the contextual information which is more and more accurate, the burden of searching for the optimal solution of the pancreatic region is well-relieved, allowing us to obtain a high-precision result. Also, this work does not rely on any pre-training model like ImageNet and relies entirely on the generalization of the model itself.

## II. METHODOLOGY

In this paper, we present a bi-directional recurrent UNet segmentation network (PBR-UNet) with the guidance of probability map, which is shown in Figure 2. PBR-UNet obtains a rough pixel-level probability map by feature extraction model, and the original image is combined with the adjacent probability graph to form a segmentation guided so that the context information can be used to limit and guide the segmentation of the current slice. Because of the interaction between adjacent slices, a chain-like correlation is formed, so we use forward and reverse loop processes to propagate context information throughout the entire segmentation process. At the same time, we use iterators to optimize the transfer process, so that each propagation can update the probability map to make it more accurate and ensure that the final output is obtained through global optimal three-dimensional information guidance. Specific details about the model will be discussed in detail below.

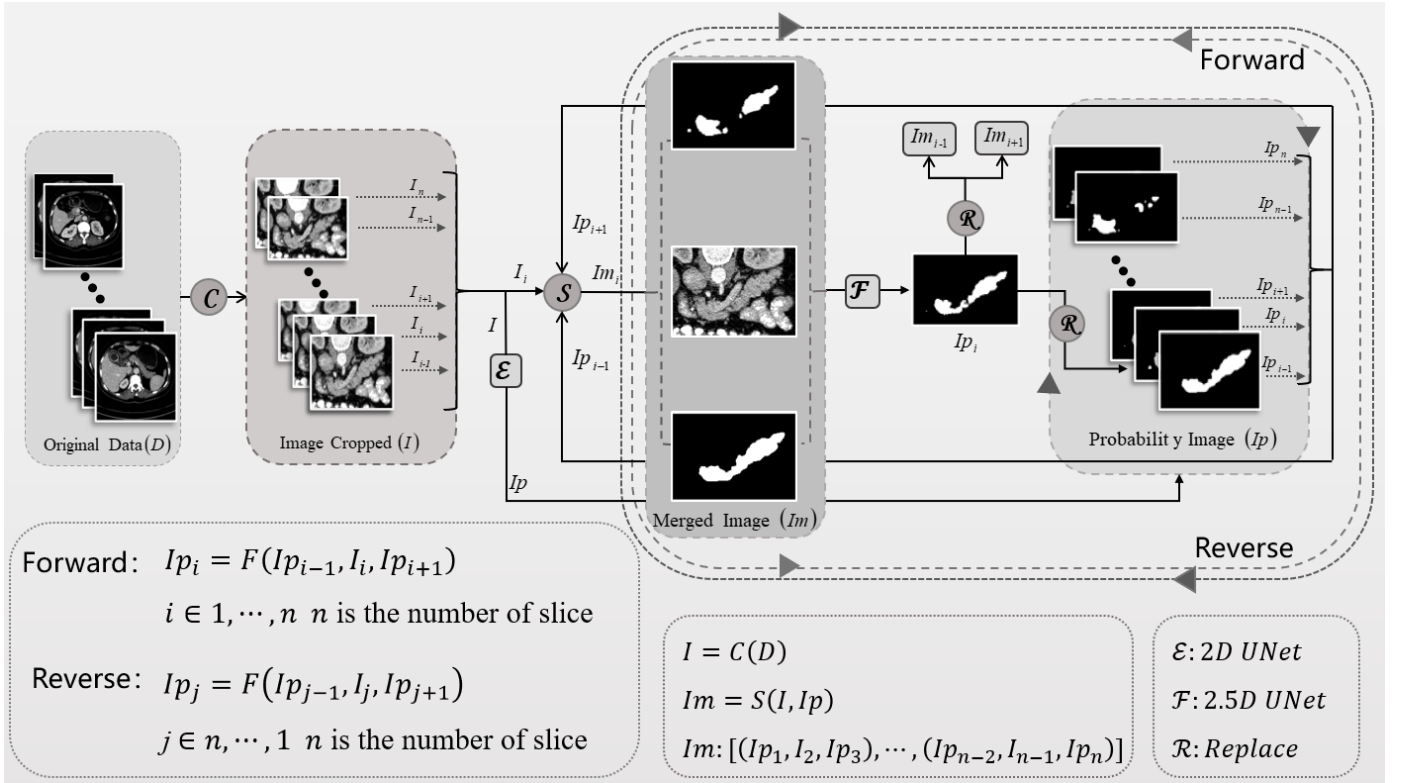


Fig. 2. The flow chart of the proposed model. The function  $E$  represents the 2D network extracted from the probability map, and the input 3D scan outputs the probability of each slice of each pixel belonging to the pancreatic tissue.  $F$  indicates that the second part carries out bi-directional recurrent segmentation.

#### A. Problem Define and Inference Schemes

Our main task is to segment the pancreas tissue from the 3D scan accurately, and the problem can be defined as follows. Given a patient's three-dimensional scan data  $P \in R^{m \times h \times w}$ , where  $m$  denotes the total number of slices,  $h, w$  respectively refers to the height and width of the image. Moreover, the data provides a fine label  $\hat{Y} \in R^{m \times h \times w}$ . We need to use this data to train a mapping function  $\Omega$  to segment the pancreas out of a given CT three-dimensional scan, to make the similarity between  $\Omega(P)$  and fine labeling  $\hat{Y}$  as high as possible. In this article, the mapping function  $\Omega$  contains two parts:  $\mathcal{E}$  and  $\mathcal{F}$ .  $\mathcal{E}$  denotes the feature extraction model, which get the pixel-level probability map of each slice in the 3D scan;  $\mathcal{F}$  denotes the bi-directional recurrent segmentation model. The threshold  $T$  is the maximum number of cycles,  $\theta$  is the threshold of evaluation, areas with a probability greater than  $\theta$  will be considered pancreatic tissue. We can use the following formula to explain the above process:

$$\mathcal{L}(\Omega, \theta, T; P, \hat{Y}) = \min \left( \frac{1}{m} \sum_{i=1}^m (\mathcal{F}(\mathcal{E}(P_i); \theta, T) - \hat{Y}_i)^2 \right) \quad (1)$$

To make full use of the 3D information of the pancreas, we combine the pixel-level probability map obtained in the feature extraction model  $\mathcal{E}$  with the original data. As shown in Figure 2, we use  $Ip$  and  $I$  to represent the probability map and the original image respectively. The data is represented by  $Im$ , and  $Im$  is used as the input to the next segmentation process  $\mathcal{F}$ . The combined multi-channel data  $Im$  have mutual influence. To introduce the three-dimensional information into the model, the

precise segmentation  $\mathcal{F}$  is designed as a bi-directional loop, which includes forward and reverse. When performing forward segmentation, the initial slice has only the information of the next slice, but no information of the last slice, the last slice is the opposite. Therefore, a two-way loop segmentation in the second step can be expressed as shown in Equation 2, and the detailed procedure will be shown in Parts B and C.

$$\Omega(P) = \sum_i (\text{reverse}_i(\text{forward}_i(P))) \quad (2)$$

#### B. Extraction and Combination of Probability Maps

We use a 2D UNet network in this process to extract the probability map. Networks with skip connections like UNet have been shown to help restore the full spatial resolution of network output. As a result, the full convolution method is suitable for semantic segmentation [10], [11]. Specifically, skipping the connection structure enables deep and shallow information to be obtained. For deep information, the semantic information of the segmentation region in the whole image can be obtained by continuous downsampling. In this paper, the positional information of the pancreatic tissue in the whole 2D slice and the geometrical shape of the surrounding tissue can be considered as the semantic information. These features can generally be used to resolve different regions. Usually, after obtaining this information, the target tissues can be roughly distinguished, it is often used in classification tasks [23], [32], [33]. However, for semantic segmentation, these features are not enough, so the skip connection used to get the shallow information is added, and the high-resolution information is

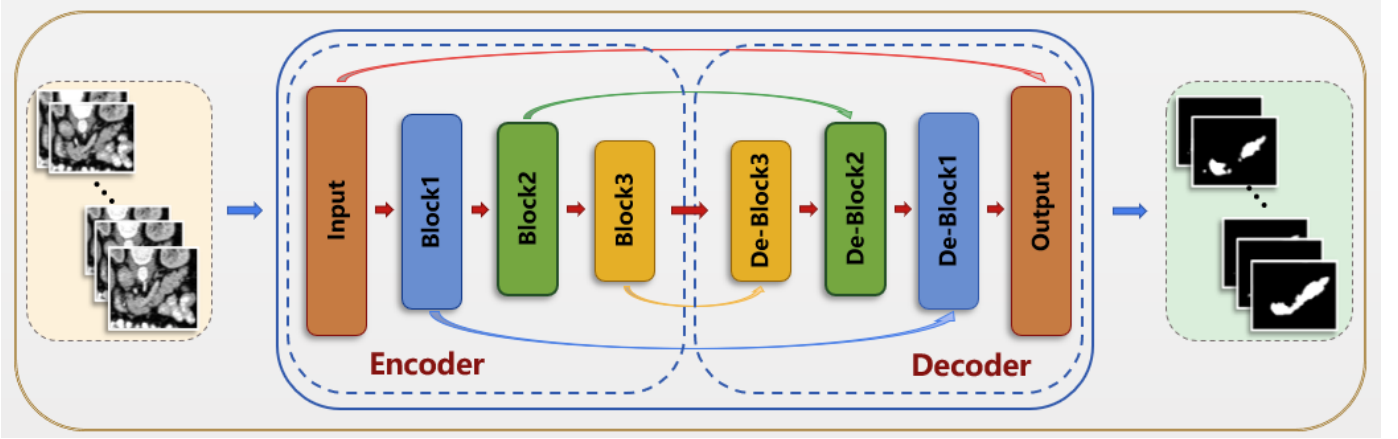


Fig. 3. Probability map extraction framework (best viewed in color). Encoder and Decoder are four layers, all of which are directly connected. The activation function is omitted, and the output layer is 1x1. Then the sigmoid activation function is used to obtain the probability that each pixel belongs to pancreatic tissue.

directly passed from the Encoder to the Decoder of the same height by skipping the connection. More fine features are available for semantic segmentation. Thus, we trained a full convolutional network with a skip connection which is proposed in [8], to quickly extract intra-slice features in 3D scans and use probability values to define them.

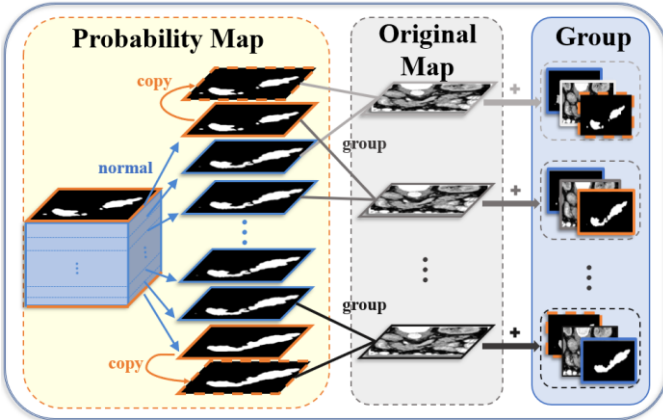


Fig. 4. Converting volume data to three-channel data. The initial slice does not have the information of the previous slice, and the last slice does not have the information of the next slice, we copy the initial slice and the last slice as their Context information.

Let  $I \in R^{m \times h \times w \times c}$  denote the input training samples, where  $c$  is the number of channels. As shown in Equation 3,  $\hat{Y}_{i,j,k,\cdot}$  denotes the fine label of the data, and the value is 0 or 1. Here 1 means that this pixel belongs to the pancreas tissue and 0 means the opposite of 1.

$$\hat{Y}_{i,j,k,\cdot} = \begin{cases} 0, & (i,j,k,\cdot) \notin \text{pancreas} \\ 1, & (i,j,k,\cdot) \in \text{pancreas} \end{cases} \quad (3)$$

Without loss of generality, we use 2D segmentation network along the Z-axis in the probability map extraction model. We do not need to get accurate binary segmentation in this step, and we only need to get the probability map  $Ip$  of each pixel. As shown in Fig 2, the function  $\mathcal{E}$  is a full convolutional network with a skip connection, which can be understood here as a conversion from volume data to a pixel-level probability map. This transformation process can be specifically expressed by the following equation:

$$Ip_{\vartheta} = \mathcal{E}(I)$$

$$I \& Ip_{\vartheta} \in R^{m \times h \times w \times c}, \|Ip_{\vartheta}\| \in [0, 1] \quad (4)$$

After obtaining the probability map  $Ip_{\vartheta}$ , the original data  $I$  and the probability map  $Ip_{\vartheta}$  are combined into three-channel data through the transformation  $S$ . [14] is to use the three slices adjacent to the original slice on the Z-axis, because the uncertainty of prediction will lose some information, which reduces the efficiency of ways to use context information. Here we replace the upper slice and the lower slice using the corresponding pixel-level probability map. This can be guided according to the probability value, therefore there will be neither absolute threshold caused by mask guidance nor uncertain loss of information. The multi-channel data obtained by the combination is denoted by  $Im_{\vartheta} \in R^{m \times h \times w \times c}$ , and the conversion process can be expressed by Equations 5, 6. It should be noted here that since the initial slice does not have the upper slice, and the last slice does not have the lower slice, we copy the initial and the final slice and add them to  $Ip_{\vartheta}$ . The process of this combination is shown in Figure 4.

$$Im_{\vartheta} = S(I, Ip_{\vartheta}), Im_{\vartheta} \in R^{m \times h \times w \times c} \quad (5)$$

$$Im_{\vartheta} = \begin{bmatrix} (Ip_{\vartheta,1}, I_1, Ip_{\vartheta,2}), (Ip_{\vartheta,1}, I_2, Ip_{\vartheta,3}), \dots \\ \dots, (Ip_{\vartheta,n-1}, I_n, Ip_{\vartheta,n}) \end{bmatrix} \quad (6)$$

2.5D UNet will segment the combined data in bi-directional recurrent under the guidance of probability map. The 2.5D network here adopts the same structure as probability map extraction model, and the number of data channels is modified to  $c$ , which is not shared with the former parameters and requires separate training. The overall structure of 2D UNet and 2.5DUNet is shown in Figure 4. Both Encoder and Decoder are four layers, and all layers are directly connected. To control the number of feature maps and prevent feature map expansion, we use the base factor  $\varpi$ , and each layer performs a multiple conversion based on the base factor  $\varpi$ . The UpSampling layer is implemented by deconvolution rather than by upsampling. Upsampling can be regarded as the reverse operation of pooling, using nearest neighbor interpolation to zoom in and directly copy the data of rows and columns to expand the size of the feature map. This method may cause the feature distribution to be abnormal [34], so we use deconvolution instead of it. The output of the deconvolution is skip-connected with the



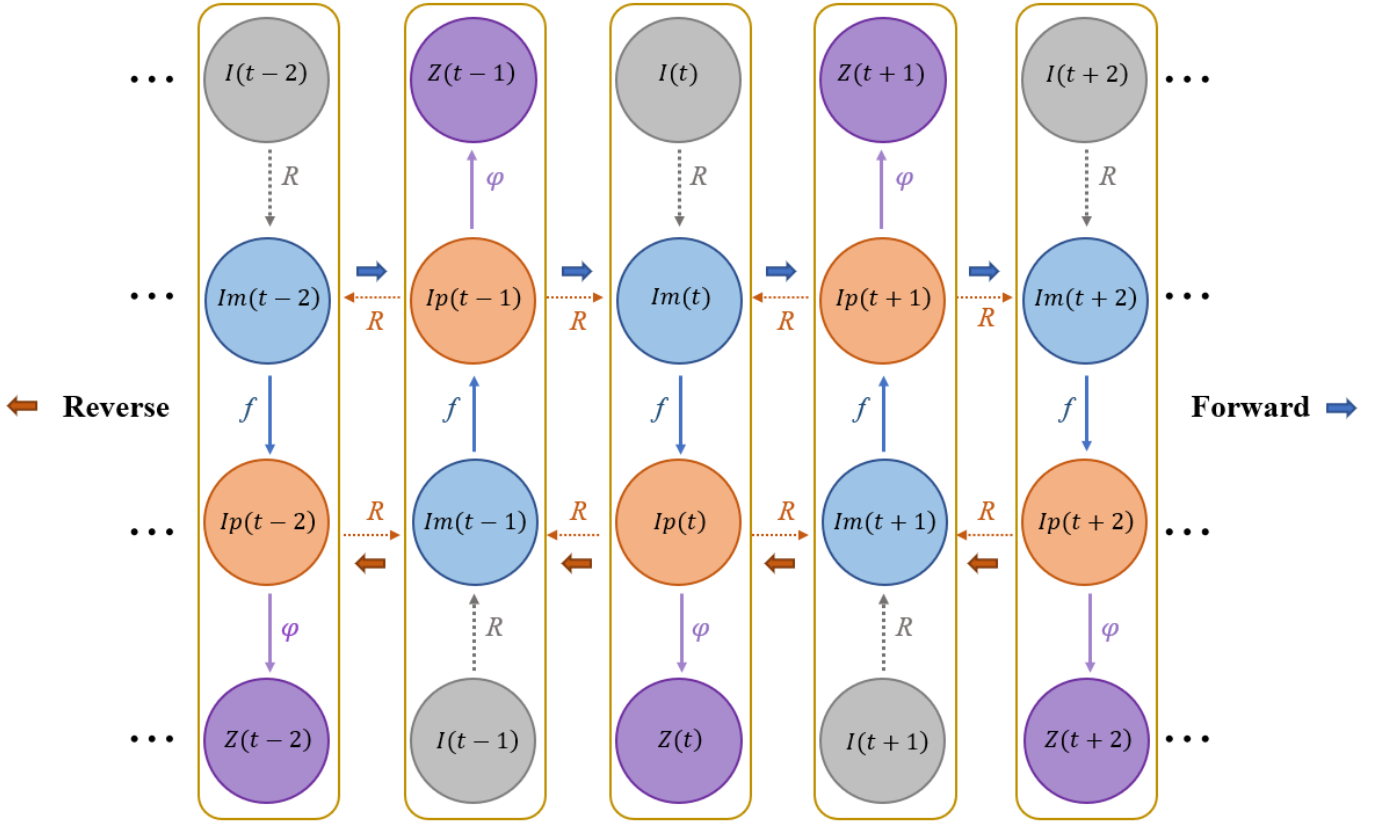


Fig. 5. The illustration of the pipeline for bi-directional recurrent segmentation. Under the guidance of the context, we can operate a single model  $f$  on all synchronization sequences of the recurrent segmentation. Without the need to set up a separate model which is synchronized with time, so that the training samples and duration required for the bi-directional recurrent model will be much less than model without parameter sharing.

corresponding shallow feature (Encoder part), then passed through two  $3 \times 3$  convolutional layers to enter the next layer. The details of the 2.5D bidirectional recurrent segmentation will be covered in more detail in the next section.

### C. Bi-directional Recurrent segmentation based on probability map guidance

A full convolution network with skip connections trained in extracting probability map can only capture intra-slice features but is powerless for the Z-axis-based contextual information that doctors use most often. What is more, 3D networks like [16]–[20], [34] have large GPU computing cost and limited kernel view and network depth [14]. Given that the pancreatic context information is shown in Figure 1 (c) is not entirely relevant, we propose to use the probability map to represent the context information in a specific range to guide the bi-directional recurrent segmentation.

In Figure 3, we show the process of how to combine the probability map with the original image. As shown in Equation 7, we will find the combination of  $Im_i$ ,  $Im_{i-1}$  and  $Im_{i+1}$  is associated on some channels, which creates a chain-like structure. Just like the principle of transmission, we hope that this structure can also transfer three-dimensional information in the network to help segmentation. We use the two-way propagation method here, and there is a spread of relevant information in two directions. Each segmentation does not lose the corresponding context information due to the loss of the propagation process. Meanwhile, two-way propagation method

also allows each segmentation process to be propagated two times. All of these can ensure that the segmentation process fully integrates the spatial information currently propagated in the network. When spatial information is chain-spread in the network, we add an iterative optimizer so that spatial information could be adjusted and optimized during the transfer process. During the propagation process, at the end of each propagation, the corresponding probability map will be updated, making the probability map more accurate, which ensures that the final output is guided by the global optimal three-dimensional information.

$$f(Ip_{i-1}, I_i, Ip_{i+1}) = f(f(Ip_{i-2}, I_{i-1}, Ip_i), I_i, f(Ip_i, I_{i+1}, Ip_{i+2})) = f(\dots) \quad (7)$$

Here we can consider the chain structure mentioned above as a recurrent neural network, just as almost all functions can be regarded as a feedforward network. Any function involving a loop can be regarded as a recurrent neural network [35]. Considering the chain structure mentioned above as a recurrent neural network has the following two advantages [35]: **a)** The model always has the same input size because it only transfers from one probability distribution state to another; **b)** We can use the same transfer function  $f$  of the same parameter on each time step. In this way, we can operate a single model  $f$  on all synchronization sequences of the recurrent segmentation, without the need to set up a separate model that is synchronized with time, so that the training samples and duration required for the recurrent model will be much less than the model without parameter sharing.

Considering that the recurrent neural network occupies a large number of resources, to reduce the resource consumption of the system, we innovatively combine the above recurrent process with 2.5D UNet and propose a bi-directional recurrent network based on pixel-level probability map guidance. Under the guidance of effective context information within a certain range, the burden of searching for the optimal solution of the pancreatic region in the fine segmentation is well-relieved. We compare our proposed model to the classical equation of the recurrent neural network, and we can regard  $Ip$  as the hidden unit  $h$  in the recurrent neural network.

$$Ip_t = f(Ip_{t-1}, Ip_{t+1}, I_t; \theta) \quad (8)$$

In the classic RNN, the hidden unit generally needs to map a sequence of a certain length  $(\dots, x_{t-2}, x_{t-1}, x_{t+1}, x_{t+2}, \dots)$  to the unit  $h_t$ , especially in statistical language modeling, it is often necessary to store all the information remaining in the sentence [35]. In the work of this article, if we map a long sequence into the current unit, it will cause the training delay to introduce noise, so we only take the adjacent slice information as the guide.

In the previous section, we introduced how to use the function  $S$  to combine the original data  $I$  and the probability map  $Ip_\theta$  into three-channel data  $Im_\theta$ . To get the binary segmentation of the final output, we first define  $\mathcal{F}[:, \theta]$  as a bi-directional recurrent 2.5D UNet network guided by probability maps, where  $\theta$  is used as a variable parameter for thresholding the output probability map  $Ip_\theta$ , which can be expressed as Equation 7. The detailed structure of the bi-directional recurrent network based on probability map guidance is shown in Table 1.

$$Z = \mathcal{A}[Ip_\theta \geq 0.5] \quad (9)$$

Now we introduce the workflow of the model. The overall algorithm flow is shown in Algorithm 1. First, we define the variables used in it. The maximum number  $T$  of bi-directional recurrent processes is  $T_{start}$  times, and the value of  $\theta$  used for thresholding is  $\theta_{start}$ .

**Forward:** When we get the combined data  $Im_\theta$  from the probability map and the original image in the probability map extractor, we use 2.5D UNet to get the new probability map  $Ip_\theta$ . The difference is that the number of model channels becomes 3. Then we use the function  $\mathcal{P}(Ip_\theta, Ip_\theta)$  to judge whether the new probability map  $Ip_\theta$  generated by the combination probability map  $Ip_\theta$  is closer to the fine label. If the improvement result is greater than 0, then we can use the newly generated probability map  $Ip_\theta$  to replace the corresponding part of the three-channel data  $Im_\theta$  generated by  $Ip_\theta$  and  $I$ , which can be expressed by the following equation, where  $Im_{\theta,i-1}^{(j)}$  represents the channel  $j$  in the data  $i-1$  in  $Im_\theta$ , and  $Ip_\theta$  will also be updated.

**Reverse:** After the network completes a forward loop, most of the  $Ip_\theta$  and  $Im_\theta$  will be updated, but the one-way loop will only get the following information and lose the information of upper slice, so we reverse the same process again, which completes a loop in the bi-directional recurrent segmentation.

$$Im_{\theta,i-1}^{(3)}, Im_{\theta,i+1}^{(1)} \leftarrow R(Ip_{\theta,i}, Im_{\theta,i-1}^{(3)}, Im_{\theta,i+1}^{(1)}) \quad (10)$$

---

### Algorithm 1: Probabilities Guided Bi-directional Recurrent

---

**Input:** input volume  $I$ , max number of iterations  $T$ , probability threshold  $\theta$ , DSC threshold  $D$ ;

**Output:** segmentation volume  $Z$ ;

```

1:  $T \leftarrow T_{start}, \theta \leftarrow \theta_{start}, t \leftarrow 0$ ;
2:  $Ip_\theta \leftarrow E(I), Ip_\theta \in R^{n \times 224 \times 224 \times 1}$ ;
3:  $Im_\theta \leftarrow S(I, Ip_\theta), Im_\theta \in R^{n \times 224 \times 224 \times 3}$ ;
4: Repeat:
5:   For  $i \leftarrow 0$  to  $n$  (forward):
6:      $Ip_{\theta,i} \leftarrow F(Im_{\theta,i}), Im_{\theta,i} = (Ip_{\theta,i-1}, I_i, Ip_{\theta,i+1})$ ;
7:     If  $\mathcal{P}(Ip_{\theta,i}, Ip_{\theta,i}) > 0$ :
8:        $Im_{\theta,i-1}^{(2)}, Im_{\theta,i+1}^{(0)} \leftarrow R(Ip_{\theta,i}, Im_{\theta,i-1}^{(2)}, Im_{\theta,i+1}^{(0)})$ ;
9:        $Ip_{\theta,i} \leftarrow R(Ip_{\theta,i}, Ip_{\theta,i})$ ;
10:    For  $j \leftarrow n$  to  $0$  (reverse):
11:       $Ip_{\theta,j} \leftarrow F(Im_{\theta,j}), Im_{\theta,j} = (Ip_{\theta,j-1}, I_j, Ip_{\theta,j+1})$ ;
12:      If  $\mathcal{P}(Ip_{\theta,j}, Ip_{\theta,j}) > 0$ :
13:         $Im_{\theta,j-1}^{(2)}, Im_{\theta,j+1}^{(0)} \leftarrow R(Ip_{\theta,j}, Im_{\theta,j-1}^{(2)}, Im_{\theta,j+1}^{(0)})$ ;
14:         $Ip_{\theta,j} \leftarrow R(Ip_{\theta,j}, Ip_{\theta,j})$ ;
15:       $Z^{[t]} = \varphi(Ip_\theta \geq 0.5)$ 
16:       $t \leftarrow t + 1$ 
17: Until  $t = T$  or  $DSC\{Z^{[t]}, Y\} \geq D$ 
```

**Return:**  $Z \leftarrow Z^{[t]}$

---

#### D. Loss Function

Since the problem we defined earlier is a two-class segmentation task with class imbalance, we use the same strategy as [20] to use Dice similarity coefficient (DSC) instead of Cross entropy for training and characterizing similarity. We give the fine label  $\hat{Y}$  and the final output  $\Omega(P)$ , then DSC loss can be defined as follows:

$$\begin{aligned} Loss(\Omega(P), \hat{Y}) &= 1 - DSC(\Omega(P), \hat{Y}) \\ &= 1 - \frac{2 \times |\Omega(P) \cap \hat{Y}|}{|\Omega(P)| + |\hat{Y}|} \end{aligned} \quad (11)$$

It can be seen from the above equation that the value of DSC loss is in the range of  $[0, 1]$ , where 0 represents the completely failed segmentation, and 1 represents the perfect segmentation.

### III. EXPERIMENTS AND RESULTS

#### A. Dataset and Pre-processing

Following previous work of pancreas segmentation [15], we also used the most authoritative public dataset NIH pancreatic segmentation dataset [6] to evaluate our approach. This data set contains 82 contrast-enhanced abdominal CT volumes and corresponding fine annotations, the resolution of each CT scan is  $512 \times 512 \times L$ , where  $L \in [181, 466]$  is the number of

sampling slices along the long axis of the body. Like [3], the images are cropped to [192,240] and fed into a probability map extraction stage. This process is represented by  $C$ . To assess the robustness of the model, we used a 4-fold cross-validation approach in this paper. Training was conducted using data from 62 (approximately 3/4) patients in randomly grouped, with the remaining 20 (approximately 1/4) being used as test data, and this random grouping will be repeated ten times. As mentioned above, we use the Dice similarity coefficient (DSC) to evaluate the model. To be more comprehensive, we measure the standard deviation, the maximum and minimum values, and the final average of all test cases.

The initial data gray value span is very large, exceeding 2000 gray values. Through prior knowledge, we cut all scanned image intensity values to the range of [-100,200] HU and normalize them to remove the interference from other tissues in the background. The value of the pancreatic region in the fine standard was then changed from 1 to 255. It is worth mentioning that our model can automatically adjust the input of different sizes, so no additional modifications are needed when inputting.

### B. Evaluation metrics

As the most common method of evaluation, we used the Dice score to evaluate pancreatic segmentation performance. Dice per case score (DC) is the score obtained by averaging the scores of each slice, and Dice global score (DG) is a calculation of the dice score after combining a patient's prediction into a 3D volume, the calculation method is shown in Formula 10. Corresponding to the Dice coefficient is Jaccard similarity coefficient (Jaccard), whose expression is  $J(X, Y) = (X \cap Y) / (|X| + |Y| - (X \cap Y))$ .

We will also use four metrics to measure the accuracy of the segmentation results, including Root Mean Square Error (RMSE), which is the square root of the ratio of the sum of the observed and true deviations to the number  $n$  of observations. The deviation between the value and the true value, the expression is shown in Equation 11; the volume overlap error  $VOE = 1 - vol(X \cap Y) / vol(X \cup Y)$ ; the relative volume difference  $RVD = vol(Y \setminus X) / vol(X)$ ; False negative,  $FN = vol(Y \setminus X) / vol(X \cup Y)$ ; False positive,  $FP = vol(X \setminus Y) / vol(X \cup Y)$ . The higher the number of Dice and Jaccard is, the better the accuracy will be; the smaller the remaining evaluation indicators are, the better the segmentation result is.

$$RMSE(x, y; \Omega) = \sqrt{\frac{1}{m} \sum_{i=1}^m (\Omega(x^i) - y^i)^2} \quad (12)$$

### C. Implementation details

In this section, we will further describe the hardware conditions, experimental environment and model details. Our network is based on the Keras framework [36]. In order to prevent the model from entering the local minimum in training, which makes it difficult to converge, we will pay attention to the changes of loss in training. If the loss does not decrease after two epochs, the learning rate  $lr$  will change according to the following formula 11-13. If the value of loss on two consecutive epochs is less than the threshold  $\delta$  (in this case,  $\delta$  is 0.0001),

the learning rate  $lr$  will be reduced to the  $(1 - \beta)$  times of the original (in this case,  $\rho$  takes 0.9).

$$\mathcal{L} = [ (|\mathcal{L}_i - \mathcal{L}_{i-1}| < \delta) \& (|\mathcal{L}_{i+1} - \mathcal{L}_i| < \delta) ] \quad (13)$$

$$\xi(\lambda) = \begin{cases} 0, & \lambda \neq 1 \\ 1, & \lambda = 1 \end{cases} \quad (14)$$

$$lr = lr - lr \times (\beta \times \xi(\mathcal{L})) \quad (15)$$

The above process is represented by the algorithm flow as follows:

---

#### Algorithm 2: The Function for Adjusting Loss

---

**Input:** loss value:  $\ell \in R^{epoch}$ , epsilon value:  $\varepsilon$ ,  
patience value:  $p$ , adjustment factor:  $\beta$ ;

**Output:** adjusted  $lr$ :  $\tilde{lr}$ ;

1:  $\varepsilon \leftarrow 0.0001, p \leftarrow 2, \beta \leftarrow 0.7, sign \leftarrow 1$ ;

2: **Repeat:**

3:  $i \leftarrow 1$ ;

4: **For**  $j$  in range of  $(i, p + i)$ :

5: **If**  $|\ell_{j-1} - \ell_j| > \varepsilon$ :

6:  $sign \leftarrow 0$ ;

7: if  $sign$  is 1 after for loop, means all loss in

8:  $(i, p + i)$  have no any drop more than  $\varepsilon$ ,

9:  $lr$  need to be adjusted.

10: **If**  $sign == 1$ :

11:  $\tilde{lr} = lr - lr \times \beta$ ;

12:  $sign \leftarrow 1$ ;

13:  $i \leftarrow i + p$ ;

14: **Until**  $i == epoch$

**Return:**  $\tilde{lr} \leftarrow \tilde{lr}$

---

We train the probability map extraction network on an NVIDIA GeForce GTX 1080Ti GPU with 11GB memory. The initial learning rate is set to  $e^{-5}$ , the batch\_size is 10, the training epoch is 450, and each epoch takes only 105 seconds. In the epoch, 1% of the samples are selected as the validation data to observe whether the training process is over-fitting. As for the bi-directional cyclic segmentation network, we use the same equipment as above to train, because the label marked by the clinician has been trained. It is accurate enough so that we will use  $(label_{i-1}, data_i, label_{i+1})$  as training data, the specific approach is consistent with the one described in the previous section B. In the relevant parameters, the batch\_size is changed to 1, the training frequency is changed to 240, and the learning rate optimization process is the same as the formula 11-13.

### D. Ablation studies

To prove that our network diagram based on probability map guidance is reasonable, we conducted different ablation experiments. We use Dice score as the criterion unless otherwise specified.

Model	Year	Min DSC	Max DSC	DICE
Roth et al., MICCAI'2015 [6]	2015	23.99	86.29	71.42±10.11
Roth et al., MICCAI'2016 [28]	2016	34.11	88.65	78.01 ± 8.20
Dou et al., MIC'2017 [15]	2017	62.53	90.32	82.25 ± 5.91
Zhou et al., MICCAI'2017 [5]	2017	62.43	90.85	82.37 ± 5.68
Zhu et al., Arxiv'2017 [18]	2017	69.62	<b>91.45</b>	<b>84.59 ± 4.86</b>
<b>ours</b>		<b>73.70</b>	91.24	83.03 ± 5.02

**The effectiveness of Probability Graph Guidance.** To test the necessity of probability map-guided segmentation, we compare it to the segmentation of 2D UNet. Under the premise of keeping the learning rate, batch\_size, epoch and other parameters unchanged, we test the accuracy of the segmentation directly after the probability map guidance is performed and without the guidance. As shown in the following figure A, in the figure, the red part indicates the part which is improved after the probability map is guided, and the yellow part indicates the result of directly using the UNet division. It can be seen from the figure that the segmentation guided by the probability map is 3%-7% higher than the Dice result directly using UNet segmentation, which indicates that the segmentation guided by the probability map can increase the accuracy of the model.

**The effectiveness of Bidirectional Cyclic Segmentation.** Although probabilistic map guidance can greatly improve the segmentation results, it cannot ensure that the context information of the whole pancreas is obtained, so we are inspired by BiLSTM to add a two-way cycle process. To prove the effectiveness of our two-way cycle, we show the results of the cycle segmentation as follows, listing the results of forward and reverse cycles once, three and five times respectively. As can be seen from the figure, after different cycles, the boundary of pancreatic tissue is much closer to the precision standard, which shows that the cycle process is effective. We use the following figure to show the relationship between the number of cycles and the accuracy of Dice. We find that after ten cycles, the results tend to be stable, that is, the model has fully learned the context information of pancreatic tissue, and the accuracy does not increase.

#### E. Compare to others on NIH pancreas dataset

The result of our segmentation is shown in Table 2. After 300 periods of training, the average DSC result of our model reached 83.02%, reaching a competitive level. The bidirectional loop guided by the probability map increases the average DSC by 2.52%, and with this structure, the worst case is mitigated.

#### F. Time consumption

Our proposed bidirectional circular network based on probability map guidance is a lightweight solution, which has not only low computational resource occupation but also low time resource overhead. We compare the experimental time of our method. We can see that we only need 8-15 s time to test a patient's result, which is much shorter than the model with refine methods such as CRF and BiLSTM.

## IV. DISCUSSION

Pancreas segmentation is of great significance for clinical computer-aided diagnosis. The segmentation results can provide accurate location and contour of the pancreas, which is helpful to the clinical diagnosis process. In this paper, we present a probabilistic graph-based pancreatic segmentation network, which aims to explore contextual information without too much irrelevant information. By validating the NIH Pancreas dataset, we have achieved a competitive result. Also, it is worth mentioning that our network has a very low cost of time resources, which is important in clinical practice, especially when a large number of 3D images (including large image size and multiple slices) are increasingly used in cumulative clinical applications [14]. We have adopted a basic 3D UNet network [19] to verify whether our computing resources can meet all requirements, and then experimented on two NVIDIA GeForce GTX 1080Ti GPU with 11GB memory. The network depth is a four-layer network with symmetrical structure. The size of the input data is  $120 \times 120 \times 120$ , but we still encountered the error of insufficient memory. By contrast, our network can work well with only one such device under the same parameters. At the same time, in terms of resource overhead, whether it is time or computing resources, the use of 3D UNet will make the overhead very large, so our method is more practical in the clinic and can save clinicians valuable time.

To better understand the validity of the model, we also compared individual patients, in which the highest accuracy can be improved 7% for patients. After observing the patient's pancreas slices, we found that there was not a much spatial correlation between the adjacent two layers of the pancreas. To verify the rigor of this method, we carried out two adjacent layers of the pancreas as a guided experiment. Compared with the performance of adjacent layers, we can see that the introduction of the adjacent two layers can increase the intensity of guidance. However, it will also introduce irrelevant interference. It is noteworthy that we found that in some cases the accuracy of certain layers of the pancreas is very low, especially in the head and tail of the pancreas. This is one of the directions we will strive for and we hope to solve the edge effect in segmentation. Due to the edge lacks part of the context information, which often leads to unsatisfactory segmentation results in several layers of experiments.



## V. CONCLUSION

We propose a bi-directional recurrent segmentation network PBR-UNet guided by probability maps for pancreas segmentation from CT volume data. This is a new way to get pancreatic context information and propagate context information to the entire network. It solves the problem of huge computational resource consumption due to the use of context information in 3D segmentation network and ignoring the Z-axis-based context information in 2D network. Finally, we validate our method on NIH Pancreas dataset and finally achieve a competitive result of 83.02%.

## REFERENCES

- [1] C. Chu *et al.*, “Multi-organ segmentation based on spatially-divided probabilistic atlas from 3D abdominal CT images,” *Lect. Notes Comput. Sci. (including Subser. Lect. Notes Artif. Intell. Lect. Notes Bioinformatics)*, vol. 8150 LNCS, no. PART 2, pp. 165–172, 2013.
- [2] R. Wolz, C. Chu, K. Misawa, M. Fujiwara, K. Mori, and D. Rueckert, “Automated abdominal multi-organ segmentation with subject-specific atlas generation,” *IEEE Trans. Med. Imaging*, vol. 32, no. 9, pp. 1723–1730, 2013.
- [3] Y. Man, Y. Huang, J. Feng, X. Li, and F. Wu, “Deep Q Learning Driven CT Pancreas Segmentation with Geometry-Aware U-Net,” no. December, pp. 0–10, 2018.
- [4] H. R. Roth, A. Farag, L. Lu, E. B. Turkbey, and R. M. Summers, “Deep convolutional networks for pancreas segmentation in CT imaging,” no. March 2015, 2015.
- [5] Y. Zhou, L. Xie, W. Shen, Y. Wang, E. K. Fishman, and A. L. Yuille, “A fixed-point model for pancreas segmentation in abdominal CT scans,” *Lect. Notes Comput. Sci. (including Subser. Lect. Notes Artif. Intell. Lect. Notes Bioinformatics)*, vol. 10433 LNCS, pp. 693–701, 2017.
- [6] H. R. Roth *et al.*, “Deeporgan: Multi-level deep convolutional networks for automated pancreas segmentation,” *Lect. Notes Comput. Sci. (including Subser. Lect. Notes Artif. Intell. Lect. Notes Bioinformatics)*, vol. 9349, pp. 556–564, 2015.
- [7] E. Shelhamer, J. Long, and T. Darrell, “Fully Convolutional Networks for Semantic Segmentation,” pp. 1–12, 2016.
- [8] O. Ronneberger, P. Fischer, and T. Brox, “U-Net: Convolutional Networks for Biomedical Image Segmentation,” pp. 1–8, 2015.
- [9] L. C. Chen, G. Papandreou, I. Kokkinos, K. Murphy, and A. L. Yuille, “DeepLab: Semantic Image Segmentation with Deep Convolutional Nets, Atrous Convolution, and Fully Connected CRFs,” *IEEE Trans. Pattern Anal. Mach. Intell.*, vol. 40, no. 4, pp. 834–848, 2018.
- [10] M. Drozdal, E. Vorontsov, G. Chartrand, S. Kadoury, and C. Pal, “The Importance of Skip Connections in Biomedical Image Segmentation,” 2016.
- [11] G. González, G. R. Washko, and R. San José Estépar, “Multi-structure Segmentation from Partially Labeled Datasets. Application to Body Composition Measurements on CT Scans,” in *Image Analysis for Moving Organ, Breast, and Thoracic Images*, 2018, pp. 215–224.
- [12] J. Cai, L. Lu, F. Xing, and L. Yang, “Pancreas Segmentation in CT and MRI Images via Domain Specific Network Designing and Recurrent Neural Contextual Learning,” no. Cv, pp. 1–11, 2018.
- [13] J. Cai, L. Lu, Y. Xie, F. Xing, and L. Yang, “Improving Deep Pancreas Segmentation in CT and MRI Images via Recurrent Neural Contextual Learning and Direct Loss Function,” pp. 1–8, 2017.
- [14] X. Li, H. Chen, X. Qi, Q. Dou, C. W. Fu, and P. A. Heng, “H-DenseUNet: Hybrid Densely Connected UNet for Liver and Tumor Segmentation from CT Volumes,” *IEEE Trans. Med. Imaging*, no. 1, pp. 1–13, 2018.
- [15] Q. Dou, H. Chen, Y. Jin, L. Yu, J. Qin, and P.-A. Heng, “3D Deeply Supervised Network for Automatic Liver Segmentation from CT Volumes,” in *Medical Image Computing and Computer-Assisted Intervention -- MICCAI 2016*, 2016, pp. 149–157.
- [16] O. Oktay *et al.*, “Attention U-Net: Learning Where to Look for the Pancreas,” no. Midl, 2018.
- [17] S. Liu *et al.*, “3D anisotropic hybrid network: Transferring convolutional features from 2D images to 3D anisotropic volumes,” *Lect. Notes Comput. Sci. (including Subser. Lect. Notes Artif. Intell. Lect. Notes Bioinformatics)*, vol. 11071 LNCS, pp. 851–858, 2018.
- [18] Z. Zhu, Y. Xia, W. Shen, E. Fishman, and A. Yuille, “A 3D coarse-to-fine framework for volumetric medical image segmentation,” *Proc. - 2018 Int. Conf. 3D Vision, 3DV 2018*, pp. 682–690, 2018.
- [19] Ö. Çiçek, A. Abdulkadir, S. S. Lienkamp, T. Brox, and O. Ronneberger, “3D U-net: Learning dense volumetric segmentation from sparse annotation,” *Lect. Notes Comput. Sci. (including Subser. Lect. Notes Artif. Intell. Lect. Notes Bioinformatics)*, vol. 9901 LNCS, pp. 424–432, 2016.
- [20] F. Milletari, N. Navab, and S. A. Ahmadi, “V-Net: Fully convolutional neural networks for volumetric medical image segmentation,” *Proc. - 2016 4th Int. Conf. 3D Vision, 3DV 2016*, pp. 565–571, 2016.
- [21] Z. Quo *et al.*, “Deep LOGISMOS: Deep learning graph-based 3D segmentation of pancreatic tumors on CT scans,” *Proc. - Int. Symp. Biomed. Imaging*, vol. 2018–April, no. Isbi, pp. 1230–1233, 2018.
- [22] Q. Jin, Z. Meng, C. Sun, L. Wei, and R. Su, “RA-UNet: A hybrid deep attention-aware network to extract liver and tumor in CT scans,” no. October, pp. 1–13, 2018.
- [23] C. Chung *et al.*, “Very deep convolutional networks for large-scale image recognition,” *Comput. Sci.*, 2014.
- [24] M. Lai, “Deep Learning for Medical Image Segmentation,” 2017. [Online]. Available: <https://arxiv.org/abs/1505.02000>.
- [25] P. F. Christ *et al.*, “Automatic Liver and Lesion Segmentation in CT Using Cascaded Fully Convolutional Neural Networks and 3D Conditional

- Random Fields,” in *Medical Image Computing and Computer-Assisted Intervention -- MICCAI 2016*, 2016, pp. 415–423.
- [26] H. R. Roth *et al.*, “An application of cascaded 3D fully convolutional networks for medical image segmentation,” *Comput. Med. Imaging Graph.*, vol. 66, no. March, pp. 90–99, 2018.
  - [27] M. Tang, Z. Zhang, D. Cobzas, M. Jagersand, and J. L. Jaremko, “Segmentation-by-detection: A cascade network for volumetric medical image segmentation,” *Proc. - Int. Symp. Biomed. Imaging*, vol. 2018–April, no. Isbi, pp. 1356–1359, 2018.
  - [28] H. R. Roth *et al.*, “Spatial aggregation of holistically-nested convolutional neural networks for automated pancreas localization and segmentation,” *Med. Image Anal.*, vol. 45, pp. 94–107, 2018.
  - [29] Q. Yu, L. Xie, Y. Wang, Y. Zhou, E. K. Fishman, and A. L. Yuille, “Recurrent Saliency Transformation Network: Incorporating Multi-Stage Visual Cues for Small Organ Segmentation,” vol. 2, 2017.
  - [30] X. Yang *et al.*, “Towards Automated Semantic Segmentation in Prenatal Volumetric Ultrasound,” *IEEE Trans. Med. Imaging*, vol. PP, no. c, pp. 1–1, 2018.
  - [31] Y. Hua, L. Mou, and X. X. Zhu, “Recurrently Exploring Class-wise Attention in A Hybrid Convolutional and Bidirectional LSTM Network for Multi-label Aerial Image Classification,” 2018.
  - [32] A. Krizhevsky, I. Sutskever, and G. E. Hinton, “ImageNet Classification with Deep Convolutional Neural Networks,” *Adv. Neural Inf. Process. Syst.*, pp. 1–9, 2012.
  - [33] M. D. Zeiler and R. Fergus, “Visualizing and Understanding Convolutional Networks,” in *Computer Vision -- ECCV 2014*, 2014, pp. 818–833.
  - [34] Y. Xia *et al.*, “3D Semi-Supervised Learning with Uncertainty-Aware Multi-View Co-Training,” 2018.
  - [35] I. Goodfellow, Y. Bengio, and A. Courville, *Deep Learning*. The MIT Press, 2016.
  - [36] F. Chollet *et al.*, “Keras,” <https://github.com/keras-team/keras>, 2015.